Dynamics of migrating sand dunes interacting with obstacles

Karol A. Bacik [1,*] Priscilla Canizares [2] Colm-cille P. Caulfield [3,1]
Michael J. Williams [2] and Nathalie M. Vriend [3,1,4]

[1]*Department of Applied Mathematics and Theoretical Physics, Centre for Mathematical Sciences,
University of Cambridge, Wilberforce Road, Cambridge CB3 0WA, United Kingdom*
[2]*Schlumberger Cambridge Research, High Cross, Madingley Road, Cambridge CB3 0EL, United Kingdom*
[3]*BP Institute, University of Cambridge, Madingley Rise, Madingley Road,
Cambridge CB3 0EZ, United Kingdom*
[4]*Department of Earth Sciences, University of Cambridge, Downing Street,
Cambridge CB2 3EQ, United Kingdom*

Wind- and water-driven migrating sand dunes frequently interact with elevated natural
and artificial topographical features. The dune-obstacle interaction can alter the migrating
behavior of the dune and, depending on the nature of the obstacle, it may generate various
societal and technological risks. Here we study the problem of dune-obstacle interaction
in a paradigmatic quasi-two-dimensional domain realized in a subaqueous laboratory ex-
periment. Generically, dunes interact with obstacles either by crossing over the obstacle or
by being trapped. We describe how the selection of these two distinct dynamical behaviors
depends on the size and shape of the obstacle, focusing in particular on the fluid flow in
the immediate vicinity of the obstacle. Specifically, we perform a modal decomposition of
the measured flow field and we discover that the outcome of the dune-obstacle interaction
is closely related to the flow structure above the obstacle.

I. INTRODUCTION

When a pile of loose sediment is exposed to sufficiently energetic wind or water current, it
spontaneously transforms into a migrating sand dune [1–3]. The course of a migrating dune can
be interrupted by a number of mobile and immobile topographical factors. First of all, it has been
shown that dunes can interact and collide with other sand dunes [4–8]. Second, dunes can interact
with various fixed natural and human-made topographical obstacles. Indeed, dune invasion is one of
the main hazards associated with infrastructure erected in sedimentary environments [2,9]. Aeolian
dunes notoriously bury roads, rail tracks, or even buildings [10–12]. Under water, dune migration
entails dredging of navigation channels and compromises the safety of subsea cables and pipelines
[13]. Despite its direct societal relevance, the problem of dune-obstacle interaction has apparently
received relatively little attention in the physical literature. To bridge this gap, in this article we
study experimentally an idealized quasi-two-dimensional (quasi-2D) interaction scenario whereby
a migrating subaqueous dune interacts with a solid obstacle.

We consider a variety of obstacles, with differing cross-sectional shapes and areas. Generically,
two qualitatively different dynamical behaviors are possible. For small obstacles, a sufficient amount
of the granular material is able to cross over the obstacle so that a dune reconstitutes on the

*Present address: Centre for Networks and Collective Behaviour, Department of Mathematical Sciences,
University of Bath, Bath BA2 7AY, United Kingdom; kab81@cam.ac.uk

downstream side of the obstacle and migrates away. Depending on the cross-sectional area and geometric shape of the obstacle, a varying quantity of the granular material is trapped in the immediate vicinity of the obstacle. Indeed, for sufficiently large obstacles, no dune re-forms on the downstream side and so the dune in its entirety may be thought of as being trapped by the obstacle. A key aim of our study is to identify and understand the controlling properties which determine whether the dune (at least partially) crosses or is (entirely) trapped after interaction with a particular obstacle. We focus on quasi-2D subaqueous sand dunes realized in an annular experimental setup. The closest natural analog of a quasi-2D sand dune is a transverse dune, but it can also be thought of as a cross section through a more complicated topography.

We begin our discussion by introducing our experimental apparatus (Sec. II). Subsequently, we use an illustrative example to discuss general features of the dune-obstacle interaction (Sec. III A) and flow around the obstacle (Sec. III B). In Sec. III C we describe qualitatively how the obstacle's shape and size, as well as the background flow velocity, impact the outcome of the dune-obstacle interaction, drawing distinction between crossing and trapped dunes. In Sec. III D we find a quantitative link between the modal structure of the flow in the immediate vicinity of the obstacle and the dividing line in parameter space between crossing and trapped dune dynamics. Finally, we summarize and discuss our conclusions in Sec. IV.

II. METHODS

A. Experimental setup

In our studies we deploy an annular flume of outer radius $R = 0.97$ m, filled with water up to $H_w = 0.45$ m [Fig. 1(a)] [4]. The working section is a $W = 0.09$ m wide channel which mimics a straight channel with streamwise periodic boundary condition ($W/R = 9/97 \ll 1$). The flow in the channel is induced by an assembly of 12 paddles of height $H_p = 0.1$ m which rotate counterclockwise at angular speed Ω_p. The paddles are partially submerged with the upper tip protruding 0.01 m above the free surface. The flume rests on a turntable, which rotates clockwise at speed Ω_t. The primary objective of this counterrotation is to create spanwise invariant quasi-2D bedforms by balancing the effects of the centrifugal force and secondary flows [14]. The flow is fully turbulent with channel-based Reynolds number Re $\sim 10^5$.

The dunes we study are made of spherical glass beads (Sigmund Lindner, Deco Beads 4504-187-LS) of nominal density $\rho_p = 2500$ kg m^{-3} and random packing fraction $\eta = 0.6$. The mean particle diameter $\bar{d} = 1.17$ mm and the material is close to monodisperse with virtually no particles with $d < 1.0$ mm or $d > 1.4$ mm. Each of the dunes initially contains $M = 2$ kg, which corresponds to a cross-section area

$$A = \frac{M}{\rho_p \eta W} = 0.0147 \text{ m}^2. \tag{1}$$

Initially, sediment is arranged into a quasitriangular heap with both sides held at the angle of repose $\beta \approx 20°$. The flow spin-up time is of order 60 s and the pile molds into its characteristic asymmetrical dune shape soon after.

Our obstacles are polystyrene cylinders and prisms wedged in at the bottom of the channel. In total we use five different shapes of different sizes; all of them are defined in Fig. 1(b). To prevent deterioration, we cover them with adhesive tape, so their surface is always smooth. In total, we conducted 15 different experiments with different obstacles and different flow rates, all of which are summarized in Table I. For each of these settings we also performed complementary flow imaging experiments (Sec. II C).

B. Topographical measurements

An ISVI IC-X12CXP camera with a 32-mm Nikon lens is positioned approximately 1.5 m away from the flume and aimed at its central axis [camera A in Fig. 1(a)]. Its field of view is a tall rectangle
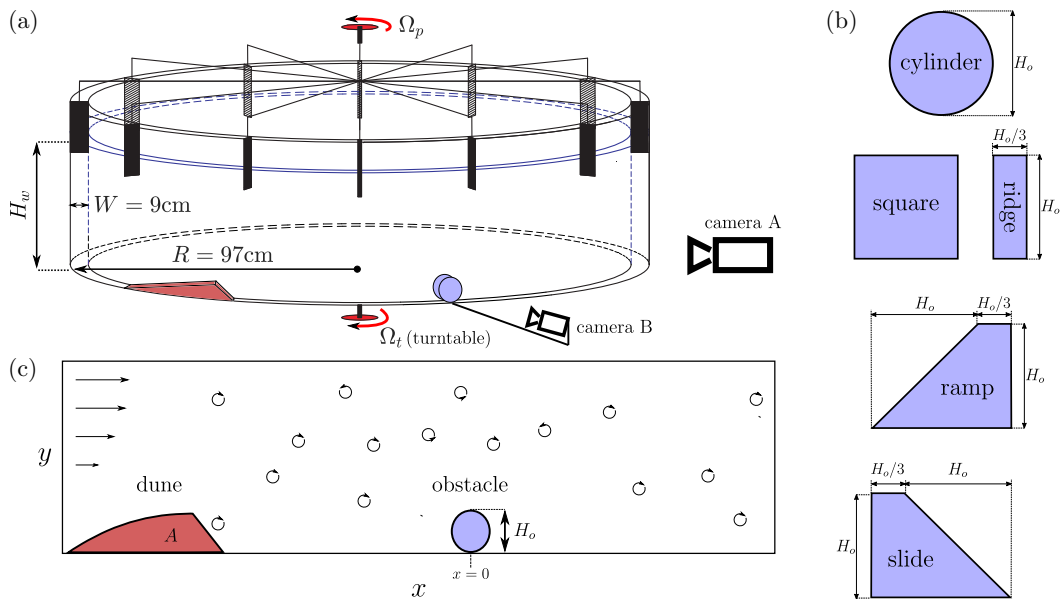
FIG. 1. (a) Experimental setup. Annular flume with a $W = 9$ cm wide working section filled with water and sediment. The motion of water is induced by an assembly of paddles rotating counterclockwise at angular speed Ω_p and the dominant direction of the flow is from the dune (red) to the obstacle (blue). The flume rests on a turntable, which rotates clockwise at speed Ω_t. The data are primarily collected with a stationary camera (A), but the sediment dynamics near the obstacle can be visualized also with an additional corotating camera (B) mounted to the turntable. (b) Obstacles: ridge, the cross section is a rectangle with aspect ratio 1:3; ramp, ridge with an upstream isosceles right triangle extension; and slide, mirror image of the ramp. In practice, both the ramp and the slide are composed of two adjoined detachable blocks. (c) System setup. In interpreting out results, we abstract the system as quasi-2D with a migrating dune of cross-section area A encroaching on an obstacle of height H_o. The origin of the coordinate system is chosen so that the centroid of the obstacle is at $x = 0$.

with a resolution of 1280×20 pixels^2, corresponding to a region of approximately 170×3 mm^2 at the outer radius of the flume, which is the location where the image is taken. The frame rate is set to 200 Hz. Appropriate uniform backlighting is provided by a cylindrical LED panel inside the annulus.

As the system rotates, every point along the circumference appears periodically in the field of view. Critically, the rotation speed is significantly faster than the speed of dune migration, so we can track the evolution of the system by reconstructing the topography of the sedimentary bed at every revolution of the turntable. Continuous recordings are not feasible when the experiment is longer than 90 min, so in some of our experiments we record only one in five revolutions (penultimate column of Table I). By using a light-intensity threshold, we identify the position of the sediment-water interface along the central pixel in each frame and the data are later postprocessed with a median filter. Due to flume imperfections, topography measurements near the bottom are noisy, so we disregard all features with topography height $h < 1.6$ cm.

C. Flow imaging

Even though the curvature and rotation of our experiment hinder precise flow imaging, we can approximate the mean velocity field using particle tracking velocimetry (PTV). To this end, we use a high-speed camera Phantom v2012 with an 85-mm Nikon lens positioned in the same location as

TABLE I. Summary of all the experiments discussed in this paper. Note that the counterrotation ratio $|\Omega_p/\Omega_t|$ is tuned empirically for each experiment to ensure a quasi-2D profile of the sedimentary bed [14]. The penultimate column ($f_{rec} = 1/n$) signifies that we made a full scan of the topography every n revolutions of the turntable.

Experiment	Obstacle shape	H_p (cm)	Ω_{tot} (rpm)	Ω_t (rpm)	Ω_p (rpm)	Duration (min)	$1/f_{rec}$ (rev)	Outcome
1	cylinder	3	13.5	−4.8	8.7	90	1	cross
2	cylinder	6	13.5	−4.8	8.7	90	1	cross
3	cylinder	9	13.5	−4.8	8.7	90	1	trap
4	square	3	13.5	−4.8	8.7	90	1	cross
5	square	6	10.5	−3.8	6.7	355	5	cross
6	square	6	11.5	−4.1	7.4	190	5	cross
7	square	6	13.5	−4.8	8.7	90	1	cross
8	square	6	15.5	−5.4	10.1	60	1	cross
9	square	9	13.5	−4.8	8.7	90	1	trap
10	ridge	6	11.5	−4.1	7.4	150	5	trap
11	ridge	6	13.5	−4.8	8.7	90	1	trap
12	ridge	6	15.5	−5.4	10.1	30	1	trap
13	ramp	6	13.5	−4.8	8.7	90	1	cross
14	slide	6	10.5	−3.8	6.7	345	5	cross
15	slide	6	13.5	−4.8	8.7	90	1	cross

the ISVI camera described in Sec. II B [camera A in Fig. 1(a)], recording with a frame rate 2000 frames/s. Its field of view is also a tall rectangle (800×128 pixels^2), which corresponds to a region of approximate size 300×6 mm^2.

All of our flow imaging experiments were conducted without sediment, but the flow was populated with neutrally buoyant Pliolite VTAC particles. For each setting (Table I), we recorded 25 videos capturing the flow in a certain fixed region in the vicinity of the obstacle. Several of them (no more than five per setting) could not be used due to file corruption. From each video we construct an instantaneous width-averaged Eulerian velocity using the DIGIFLOW software package [15]. Finally, by averaging the images we construct an ensemble- and depth-averaged velocity field $(\bar{U}(x, y), \bar{V}(x, y))$ (cf. Sec. III B). We use the azimuthal component of this velocity field $\bar{U}(x, y)$ to quantify various features of the flow below, in Sec. III B.

D. Qualitative visualization of sediment transport

Our setup also gives the opportunity of filming the bed with a corotating camera mounted 7 cm away from the outer wall of the flume looking inward at the channel [Camera B in Fig. 1(a)]. The device we use is a compact battery-operated travel camera (Lumix DMC-TZ40). It records at a frame rate of 25 Hz and we use it to visualize the qualitative features of the bed in the vicinity of the obstacle. It is important to note that, due to the battery and memory constraints, this camera is not able to record the experiment continuously.

III. RESULTS

A. Qualitative example

To introduce the physical nature of the dune-obstacle interaction we will now analyze an example experiment, which we will also use as a vehicle to define various quantities of interest. Our selected example is experiment 2 from Table I, lasting 90 min. Its entire course is presented in Fig. 2 in the form of a space-time diagram. As the domain is periodic, the spatial coordinate x is parametrized with angle $\theta \in [-\pi, \pi)$ so that $x = R\theta$. The coordinate system is defined so that the centroid of
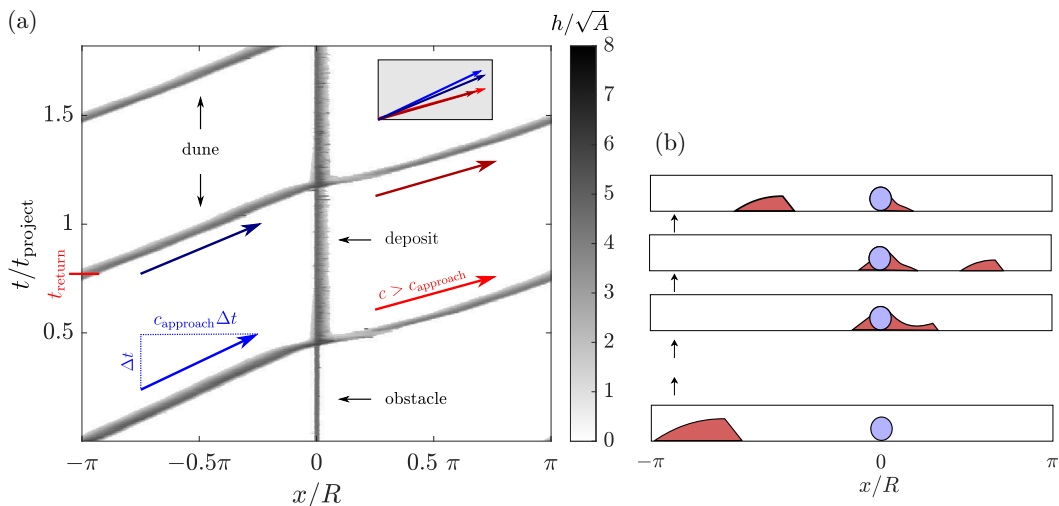
FIG. 2. Example experiment with a cylinder of diameter $H_o = 6$ cm located at $x = 0$. (a) Space-time diagram showing a migrating dune interacting with and crossing the solid obstacle. The inset allows us to compare the dune speed c at different points of the experiment (to be precise, the arrows correspond to appropriate linear fits for $x \in [-0.75, -0.25]\pi R$ or $x \in [0.25, 0.75]\pi R$). Note that a vertical arrow would correspond to $c = 0$. (b) Schematic showing the progress of a crossing interaction.

the obstacle is located at $x = 0$. At the start of the experiment, the dune is placed at the opposite side of the annular region, at $x = -\pi R$. In this particular experiment, the obstacle is a cylinder of diameter $H_o = 6$ cm resting on the floor, its axis aligned with the radial direction of the flume. The grayscale of Fig. 2 corresponds to the topographical height $h(x, t)$. Even though the imaging technique does not make a distinction between the dune and the obstacle, we can easily distinguish the fixed obstacle centered at $x = 0$.

After initial rearrangement, the dune approaches the obstacle with a close-to-constant migration speed $c_{\text{approach}} = 7.4$ m/h. According to classical theory, the migration rate of a quasi-2D steady-state dune is given by

$$c = \frac{\Delta Q}{H_d}, \tag{2}$$

where ΔQ is the difference in sand (area) flux between the crest and the upstream edge and H_d is the height of the dune [1,3,16].

The value of c_{approach} was computed by fitting a straight line to the crest position $x_c(t)$, restricted to the interval $x_c \in [-0.75\pi, -0.25\pi]R$. The crest is the tallest point on the dune and it is unambiguously defined as long as the dune is away from the obstacle. In Sec. II C we will discuss what controls the value of c_{approach}. Throughout this paper we will use

$$t_{\text{project}} = \frac{2\pi R}{c_{\text{approach}}} \tag{3}$$

as a characteristic timescale. It is a projected return time based on the behavior of the dune on approach, i.e., if it were not for the obstacle, the dune would complete one full revolution around the flume within t_{project} (in this example $t_{\text{project}} \approx 50$ min). As we can see, the presence of the obstacle effectively speeds up the dune, so now the dune returns to $x = \pi R$ at $t_{\text{return}} \approx 0.75 t_{\text{project}}$.

At $t \approx 0.45 t_{\text{project}}$, the dune comes into close proximity to the obstacle and a (crossing) interaction ensues. Figure 3 shows close-up photographs of the dune-obstacle collision taken with a corotating camera mounted to the turntable [camera B in Fig. 1(a)]. For technical reasons, these images
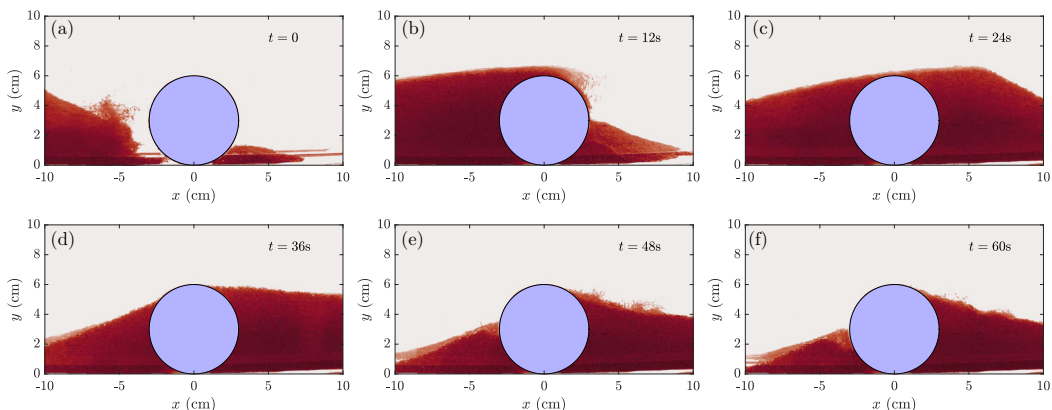
FIG. 3. Close-up photographs of a crossing dune-obstacle interaction taken every 12 s with a camera mounted to the turntable [camera B in Fig. 1(a)]. For visualization purposes, the obstacle is masked in blue and the rest of the image is printed in false color. (a) The dune approaches the obstacle. Note that a small amount of sediment swept away from the dune has already accumulated in the downstream recirculation region. (b) The downstream region gradually fills with sediment as the dune crosses the obstacle. (c) At some point, the obstacle is fully buried by the dune. (d)–(f) The dune's crest moves away from the field of view. Upstream and downstream deposits form and gradually shrink.

correspond to a different realization of the same experiment and the times indicated in Fig. 3 are not calibrated with Fig. 2. Note that the spatial extent of the x axis in Fig. 3 Δx is approximately 20 cm. If it were not for the obstacle, the dune's crest would traverse this extent in $\Delta t = \frac{\Delta x}{c_{\text{approach}}} = 97$ s, but Fig. 3 shows that in the presence of the obstacle, the same traverse only takes about 30 s. The reason for this significant speedup is partly geometric (the sedimentary layer passes through a contraction) and partly dynamic (the fluid speeding up around the obstacle increases sediment flux). Interestingly, Fig. 3(c) shows that at a certain stage of the dune's crossing the obstacle is fully buried. At this stage the obstacle is dynamically cloaked, i.e., for all intents and purposes the bed dynamics is equivalent to that of a bigger dune. Nevertheless, after several seconds, the surface of the obstacle is exposed on the upstream side by the flow again and we can see a particular bed shape forming both upstream and downstream of the obstacle [Figs. 3(d)–3(f)]. The upstream deposit shrinks and by consulting Fig. 2 we can verify that after 10 min the deposit is completely eroded away, with all the granular material having crossed the obstacle.

The evolution of the downstream deposit is slightly more complicated. Transiently, it forms an elongated sheet stretching from the obstacle to the downstream edge of the dune, but eventually the sheet pinches off and divides into two parts [Fig. 2(b)]. The downstream portion of sediment forms an isolated migrating dune and the upstream portion is retained in the immediate downstream vicinity of the obstacle, showing that even when all the dune material crosses an obstacle, it is possible for the actual dune to be smaller when it re-forms and migrates downstream.

As we can see in the inset in Fig. 2, the migration rate of the dune which recovers downstream is significantly larger than c_{approach}, but it decelerates as it moves away from the obstacle. The physical origin of this change is speed is twofold. First of all, after crossing the obstacle the dune is exposed to intense turbulent eddies shed off the upstream obstacle which enrich the sediment flux, i.e., increase the numerator of (2) [4]. Their strength decays away from the obstacle, which is one reason for the dune deceleration. Second, the recovery dune is smaller [cf. the denominator of (2)], as a small amount of sediment is permanently trapped by the obstacle. Nevertheless, as part of the near-obstacle residue is slowly eroded away, it gradually gains mass, which is the other reason for deceleration. The downstream deposit is never completely eroded away, so at the second approach the dune is slightly smaller (and therefore faster) than it was at the first approach. However, the
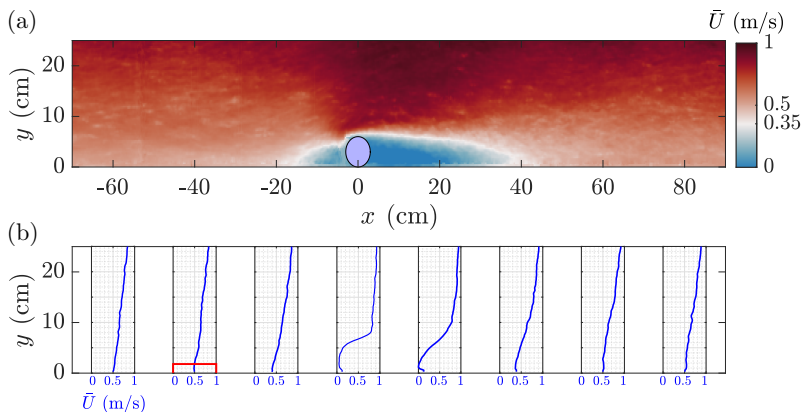
FIG. 4. Example PTV measurements. (a) Ensemble-averaged azimuthal velocity $\bar{U}$ around a cylinder with $H_o = 6$ cm. Note the flow speedup above the obstacle and the momentum deficit in the wake. (b) Each inset shows the velocity profile $\bar{U}(y)$ averaged for $x \in [x_0 - 5 \text{ cm}, x_0 + 5 \text{ cm}]$, where $x_0 \in \{-60 \text{ cm}, -40 \text{ cm}, -20 \text{ cm}, 0 \text{ cm}, 20 \text{ cm}, 40 \text{ cm}, 60 \text{ cm}, 80 \text{ cm}\}$. For the region corresponding to the obstacle, we set $\bar{U} = 0$. The red box of size 10×2 cm^2 corresponds to the region near $x = -40$ cm where we define u_{incid}.

deposition after subsequent crossings does not appear to be larger than it was after the first crossing. Therefore, after the second crossing, the dynamics is almost identical to that after the first crossing, so after the second crossing the process would just repeat periodically. In other words, while the first crossing is distinctly different, it has been verified that the nth crossing is nearly identical for all $n \geqslant 2$.

B. Flow measurements

Apart from the topographical record of the dune-obstacle interaction, we also estimate the mean velocity field $(\bar{U}, \bar{V})$ around each of the obstacles in the absence of the dune. The details of this procedure are explained in Sec. II C. Figure 4 shows the azimuthal velocity field for our example obstacle (experiment 2). Away from the obstacle, the velocity profile we measure is close to linear, but it is significantly altered in the vicinity of the obstacle. Above the obstacle, there is a significant flow speedup and both upstream and downstream of the obstacle we can observe zones of depleted momentum. Although the PTV technique is not able to resolve the details of the downstream wake, in the experiment we also observe a clear recirculation bubble forming downstream of the obstacle. In Sec. III D we will analyze the differences in the flow patterns around different obstacles in more depth. However, before we proceed we need to make an important technical remark about the incident flow upstream of the obstacle.

Incident speed

We quantify the upstream boundary conditions with incident surface velocity u_{incid}, which is defined as a spatiotemporal average of $\bar{U}$ in a particular wall-attached interrogation window located at a fixed distance upstream of the obstacle [Fig. 4(b)]. As the PTV technique is not able to resolve the thin boundary layer due to resolution constraints, u_{incid} is far from zero. As expected, u_{incid} is an increasing function of Ω_{tot}, which is the counterrotation speed of the driving assembly [Fig. 5(a)]. However, for fixed Ω_{tot} we also see systematic differences between different obstacles. Figure 5(a) shows that u_{incid} is smaller for the obstacles which are big and sharp (e.g., ridge). This is because the velocity distribution at the bottom wall is a function not only of the velocity prescribed at the top, but also of the surface roughness. Thus, if an obstacle imposes significant form drag, the mean
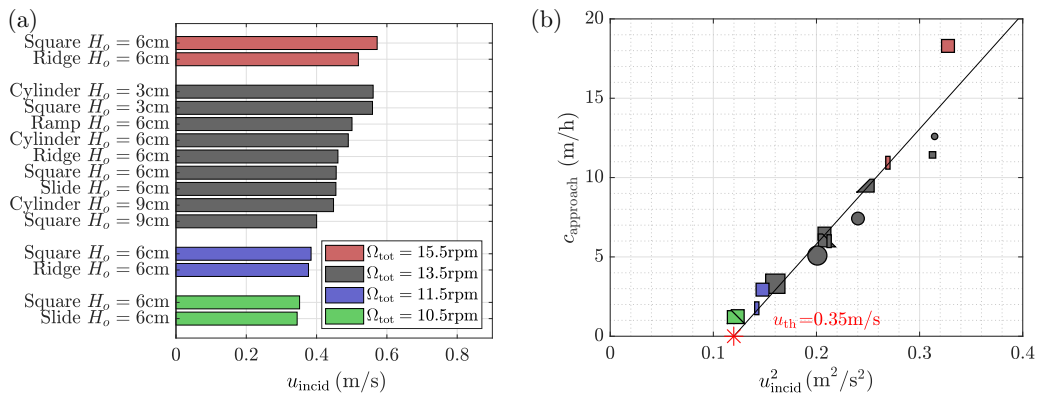
FIG. 5. Incident speed. (a) Incident speed measured for different obstacles, under flow conditions defined in Table I, but without any sediment in the tank. Note that apart from Ω_{tot}, u_{incid} is strongly affected by the size and shape of the obstacles. For fixed Ω_{tot}, the figure can be interpreted as a ranking of obstacles, from least disruptive (small, blunt) to most disruptive (big, sharp). (b) The incident speed is monotonically related to the dune approach speed. Here we fit an empirical law (4). The symbols in (b) are colored with the rotation speeds as shown in (a), with symbol shape and size being related to the particular obstacle used in the relevant experiment.

azimuthal velocity will be reduced. In some sense, the effect of a sharp obstacle fixed at the bottom is analogous to having an additional blade rotating in the opposite direction to the flow-inducing driving paddles.

The differences in the incident fluid velocity u_{incid} explain the differences in dune approach speed $c_{approach}$. According to the formula (2), for fixed dune height the migration rate is directly proportional to the differential sediment flux ΔQ, which in turn is a function of the shear stress exerted on the sedimentary bed. A linearized transport law would assume that sediment flux is proportional to the excess shear stress, which in turbulent flows can be expressed as a quadratic function of appropriate velocities [2,17]. Even though u_{incid} is not necessarily the most appropriate velocity, Fig. 5(b) shows that the differences in $c_{approach}$ between different experiments are indeed well described by an empirical relation

$$c_{approach} \propto u_{incid}^2 - u_{th}^2, \tag{4}$$

where we fit $u_{th} = 0.35$ m/s. In summary, even though the dune is always of the same size, the approach speed $c_{approach}$ varies between different experiments, and we can explain the differences by measuring the fluid velocity near the bottom wall.

C. Crossing-trapping transition

In Sec. III A we described a dune-obstacle interaction, where, despite some mass reduction, the dune recovered downstream as a coherent migrating structure. This regime, which we refer to as obstacle crossing or simply crossing, is one of the two possible outcomes of the dune-obstacle interaction. The alternative will be referred to as dune trapping, or simply that the dune is trapped. In this regime, the sediment capture is not partial, but complete, and the dune does not re-form downstream.

In this section we describe qualitatively the impact of obstacle size (Sec. III C 1), obstacle shape (Sec. III C 2), and the background flow speed (Sec. III C 3) on the outcome of the dune-obstacle interaction (i.e., crossing or trapping). In Sec. III D we will relate these results to the flow structure around the obstacle in a quantitative manner.
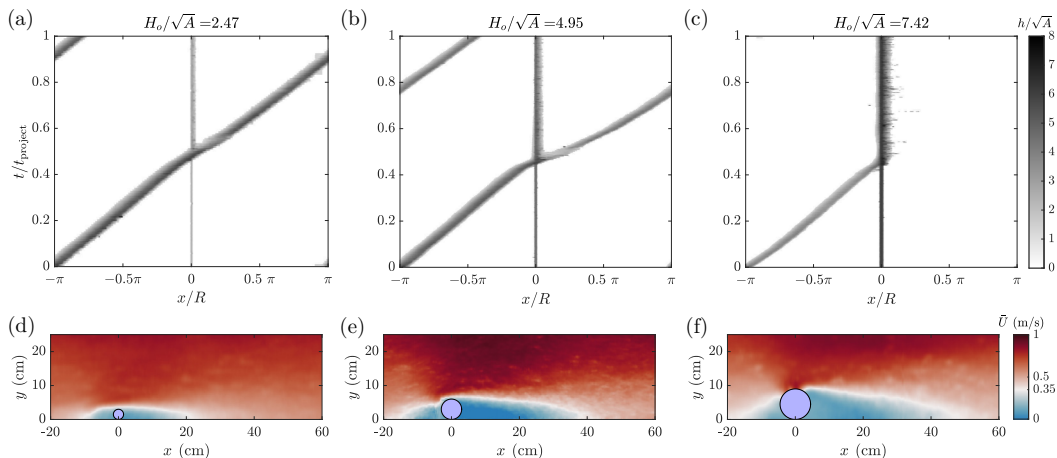
FIG. 6. Dune-cylinder interaction for (a) $H_o = 3$ cm (experiment 1), crossing; (b) $H_o = 6$ cm $\approx H_d$ (experiment 2), crossing; and (c) $H_o = 9$ cm (experiment 3), trapping. (d)–(f) PTV-measured field for the corresponding experiments showing that the size of the wake region increases with H_o.

1. Size effects

The outcome of the dune-obstacle interaction is first and foremost controlled by the size ratio

$$\eta = H_o/\sqrt{A}. \tag{5}$$

As $\eta \to 0$, the obstacle becomes indistinguishable from the surface roughness, so the dune can cross it almost uninterrupted. Conversely, if $\eta \gg 1$, the obstacle plausibly blocks the motion of the dune, thus trapping all the granular material in the immediate vicinity of the obstacle. That is indeed what we observe for both cylindrical (Fig. 6) and square obstacles (Fig. 7). In Figs. 6(a) and 7(a) the height of the approaching dune H_d is significantly larger than H_o, in Figs. 6(b) and 7(b) $H_d \approx H_o$, and in Figs. 6(c) and 7(c) $H_d < H_o$. Nevertheless, the aspect ratio of the dune is not constant, so we will continue to use η instead of H_o/H_d. For both cylinders and squares, the dune crosses the
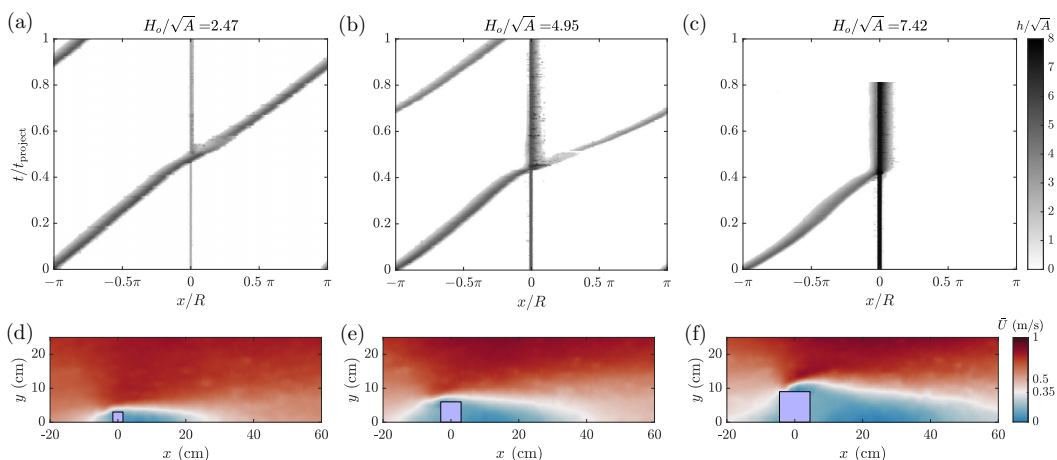

FIG. 7. Dune-square interaction for (a) $H_o = 3$ cm (experiment 4), crossing; (b) $H_o = 6$ cm $\approx H_d$ (experiment 7), crossing; and (c) $H_o = 9$ cm (experiment 9), trapping. (d)–(f) PTV-measured field for the corresponding experiments showing that the size of the wake region increases with H_o (cf. Fig. 6).
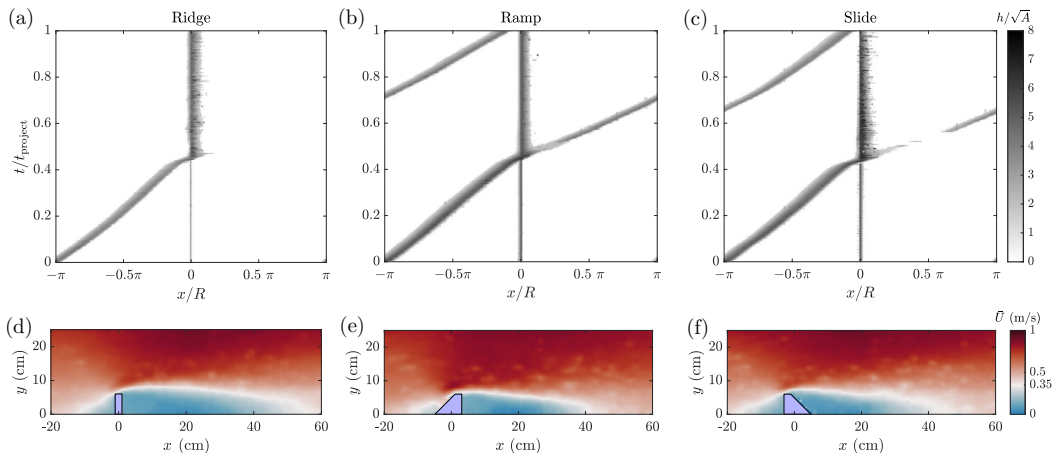
FIG. 8. Shape effects. (a) Ridge of height $H_o = 6$ cm traps the migrating dune (experiment 11). The outcome can be changed by appending (b) a ramp (experiment 13) or (c) a slide (experiment 14). See Fig. 1(b) for the definition of the shapes. The gap in data in (c) near $x = 0.5\pi R$ indicates that the transient bedform was so flat that it fell below our noise level $h = 1.6$ cm. (d)–(f) The differences between the three experiments can be related to the PTV measurements. The turbulent wake forming downstream of the ridge is larger than the ones behind the ramp or the slide.

two smaller obstacles and it is trapped by the obstacle with $\eta = 7.42$, as illustrated in Figs. 6(c) and 7(c).

As expected, the smaller the obstacle, the less effect it has on the course of the migrating dune. This can be quantified by looking at the ratio of the actual return time t_{return} and the projected return time t_{project}. For example, for the small square ($H_o = 3$ cm) $t_{\text{return}} \approx 0.9 t_{\text{project}}$ and for the larger square ($H_o = 6$ cm) $t_{\text{return}} \approx 0.7 t_{\text{project}}$ [Figs. 7(a) and 7(b)]. As previously noted, in the absence of an obstacle $t_{\text{return}} = t_{\text{project}}$, and small values of the ratio $t_{\text{return}}/t_{\text{project}}$ correspond to large distortions in the projected trajectory.

2. Shape effects

Based on the considerations of the preceding paragraph, one may postulate the existence of a critical size ratio η_{crit} which delimits the crossing-trapping boundary. We find, however, that η_{crit} also is a function of the obstacle shape. For example, by comparing Figs. 6 and 7 we can observe that for fixed H_o, t_{return} is smaller for the squares than for the cylinders. This indicates that squares are more capable of trapping sediment than cylinders, which suggests that η_{crit} is larger for cylinders.

A more striking example is provided in Fig. 8(a), where the obstacle is a ridge of height $H_o = 6$ cm ($\eta = 4.95$). Although the dune was able to cross both square and cylindrical obstacles of the same height, it is clearly trapped in the wake of the ridge. This illustrates the important point that trapping does not correspond simply to the granular material piling up on the upstream side of an obstacle. It is also possible that granular material crosses over the obstacle, but is then trapped sufficiently close to the obstacle in the downstream lee so that the dune is not observed to reorganize into a coherent form and migrate away. Interestingly, the subtle interplay between the granular material and the upstream and downstream flow near to the obstacle is illustrated further by the observation that the trapping propensity of the ridge is mitigated by appending to it either an upstream ramp or a downstream slide. Note that for different shapes the flow structure around the obstacle is different. In particular, Figs. 8(d)–(f) indeed show that the influence of the ridge, which is the sharpest obstacle, extends further downstream than in the case of either the ramp or the slide, thus making downstream trapping more likely to occur.
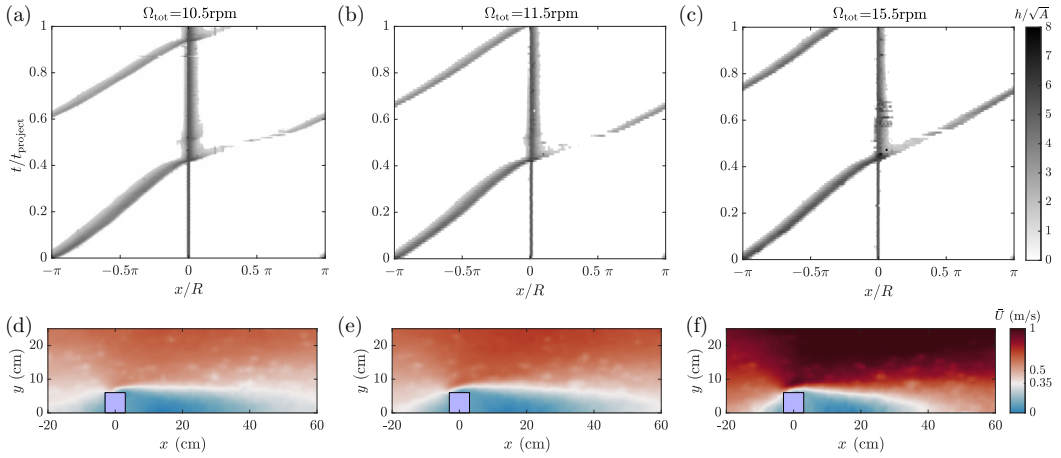
FIG. 9. Flow speed effects. In all the panels, the obstacle is a square with $H_o = 6$ cm. The return time t_{return} increases as we increase counterrotation rate Ω_{tot} from (a) 10.5 rpm (experiment 5) through (b) 11.5 rpm (experiment 6) to (c) 15.5 rpm (experiment 8). Note that an intermediate case (13.5 rpm) has already been presented in Fig. 7(b). (d)–(f) PTV measurements confirm that the average azimuthal velocity of the fluid increases with Ω_{tot}. This increase correlates with the increase in the dune migration rate and so t_{project} is approximately 14 times larger in (a) than in (c).

3. Flow speed effects

Some systematic differences are also observed as we vary Ω_{tot}, which controls the ambient flow conditions and therefore the intensity of sediment flux (Fig. 9). Figure 10 shows that for squares with $H_o = 6$ cm, t_{return} decreases with the incident speed u_{incid}, i.e., as the sediment transport diminishes, it is more difficult for the dune to cross the obstacle. This effect, however, is surprisingly weak. In particular, within the constraints of our experimental parameters, we have not been able to change
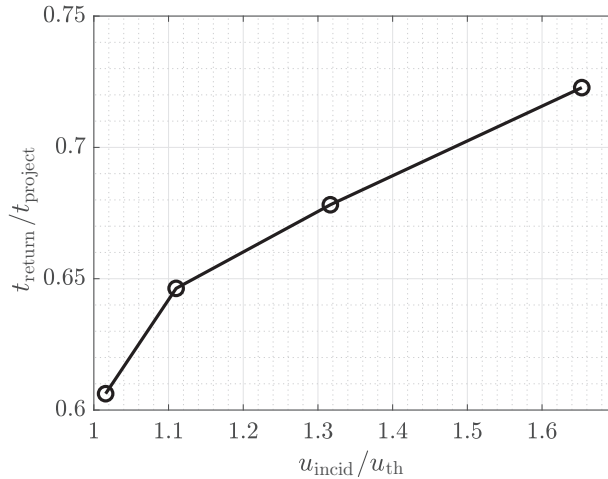

FIG. 10. Return time for the dune crossing the square with $H_o = 6$ cm (experiments 5–8) plotted as a function of the incident flow speed u_{incid}. Small values of $t_{\text{return}}/t_{\text{project}}$ correspond to strong interruption of the migrating dune. Note that t_{return} is always lower than t_{project} and there is an approximate lower bound $t_{\text{return}} > \frac{1}{2}t_{\text{project}}$ (note that by construction the dune collides with the obstacle at $t \approx \frac{1}{2}t_{\text{project}}$).

the binary outcome of the dune-obstacle interaction. The dune always traverses the square and the slide with $H_o = 6$ cm and it is always trapped by the ridge of the same height.

D. Relating the outcome of a dune-obstacle interaction to the flow structure

The preceding section can be summarized by saying that the outcome of the dune-obstacle interaction depends strongly on the size and shape of the obstacle and weakly on the background fluid velocity. Now we will attempt to synthesize these findings by relating them to the flow field measurements.

Our aspiration to explain the outcome of the dune-obstacle interaction from the PTV measurements is motivated by a pragmatic quest for an inexpensive diagnostic which would give an indication of the most likely outcome. In reality, the dynamics is far more complex. In particular, when the dune collides with the obstacle, the velocity field is significantly altered and the course of the interaction is controlled by the mutual feedback between the topography and the fluid flow. Therefore, our PTV measurements, conducted in the absence of a dune, almost certainly do not capture all the relevant physics. Nevertheless, as we will see, they still encode some highly relevant information.

In lack of an obvious quantitative relationship between the averaged velocity field $(\bar{U}, \bar{V})$ and the dune-obstacle interaction, we adopt a data-driven methodology. Specifically, we employ principal component analysis (PCA) [18]. To this end, for each of the 15 experiments (see Table I), we discretize the azimuthal velocity field $\bar{U}_i(x, y)$ $(i = 1, \ldots, 15)$ in $x \in [-70, 90]$ cm $\approx [-0.23, 0.30]\pi R$ and $y \in [0, 25]$ cm $\approx [0, 21]\sqrt{A}$ using a 200×40 regular grid. Thus, we can treat each velocity field $\bar{U}_i$ as a point in a space of dimension $8000 = 200 \times 40$. Using the whole ensemble of the data points, we perform singular value decomposition to compute the principal components (principal modes) $\hat{u}_j$ $(j = 1, \ldots, 15)$ so that each data point can be represented as

$$\bar{U}_i = \sum_{j=1}^{15} \alpha_{ij} \hat{u}_j, \tag{6}$$

where we refer to α_{ij} as the weights. The principal modes $\hat{u}_j$ are ordered based on their energy content, which is quantified by the singular value

$$\sigma_j = \sqrt{\sum_{i=1}^{15} \alpha_{ij}^2} \tag{7}$$

(Fig. 11). We will now focus on the first two most energetic modes.

As the data have not been centered, σ_1 is significantly larger than all the other singular values and the leading first principal component $\hat{u}_1$ is closely related to the mean of all the flow fields [Fig. 12(a)]. The first principal component $\hat{u}_1$ is everywhere positive and the corresponding weights α_{i1} correlate with the incident speed u_{incid} [Fig. 12(e)]. As noted in Sec. III C 3, the outcome of the dune-obstacle interaction depends only weakly on the ambient velocity, so it cannot be predicted from either α_{i1} or u_{incid}.

Of greater interest is the second principal mode $\hat{u}_2$, which is a superposition of a simple shear and a localized retardation above and downstream of the obstacle. Interestingly, the associated weights α_{i2} are strongly related to the outcome of the dune-obstacle interaction. First of all, there is a threshold α_2^* which perfectly separates the trapping experiments from the crossing experiments [red dashed line in Fig. 12(d)]. The trapping events correspond to high values of $\alpha_{i2} > \alpha_2^*$ and the crossing events to $\alpha_{i2} < \alpha_2^*$. The specific value of α_2^* is certainly a function of the dune cross-section area A and we hypothesize that α_2^* would be larger for larger dunes. Moreover, among the crossing experiments, the value of α_{i2} is negatively correlated with the return time ratio $t_{\text{return}}/t_{\text{project}}$ [Fig. 12(f)].
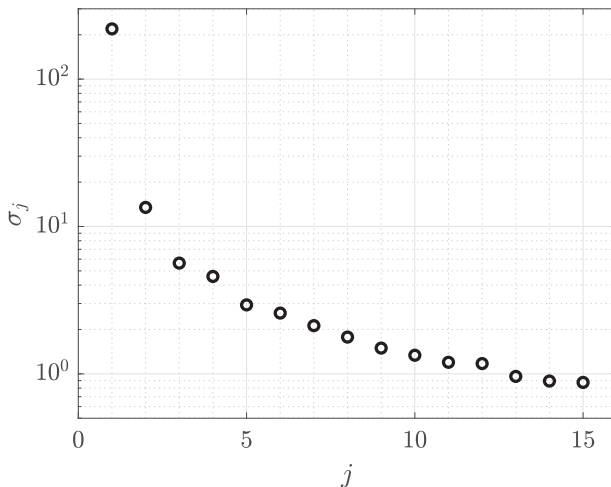
FIG. 11. Singular values ordered by magnitude. The leading singular value is larger by an order of magnitude as the data have not been centered.

It has been verified that this trend is insensitive to the details of the discretization grid. We can also obtain a similar result using the mean-centered version of the PCA or if the modes are constructed using a subsample of the data. It is important to emphasize that, as a data-driven method, PCA is completely ignorant of the sand dune context, but our result has a plausible physical interpretation. Indeed, it is conceivable that an intense flow structure with negative horizontal velocity [Fig. 12(b)] promotes sediment trapping.

Unsurprisingly, the smallest obstacles (experiments 1 and 4) have the largest value of the ratio $t_{\text{return}}/t_{\text{project}}$, as such obstacles perturb the flow the least. As is apparent in Fig. 12(f), this very small perturbation is associated with a large negative weight for the second principal component. This large negative weight has the main effect of canceling out the downstream wake structure of the first principal component [as is apparent in Fig. 12(a)], thus leading to a (largely) unperturbed velocity structure.

IV. DISCUSSION

In this paper we have studied the interaction of a migrating sand dune interacting with a solid obstacle in a paradigmatic quasi-2D setting. Quasi-2D bedforms of our experiments obviously lack the complexity of their 3D analogs, but we believe that understanding quasi-2D interactions is an important first step towards understanding more complicated scenarios. It is also an open question to what extent our results can be extrapolated to aeolian dunes, where the saturation length can be comparable to (or indeed greater than) the size of the obstacle.

Our experiments revealed that the dune-obstacle interaction can produce two qualitatively distinct outcomes which we classified as crossing and trapping. We have shown that a dune is more likely to be trapped in the wake of the obstacle if the dune-to-obstacle size ratio η is small. We have also found that when $\eta = O(1)$, the outcome of the interaction may depend on the shape of the obstacle. Smooth obstacle shapes (e.g., cylinders) promote crossing and sharp obstacles (e.g., ridges) are more likely to trap the dune. If dune crossing is a desired outcome, this principle should be taken into consideration in designing subsea infrastructure. From an academic point of view, the strong dependence of the interaction type on the shape of the obstacle opens an interesting class of optimization exercises [19]. We have also found that the ambient flow velocity can affect the outcome of the dune-obstacle interaction as well, but in our experiments this effect was relatively weak. In summary, we have found that the dune is more likely to be trapped if the obstacle is large
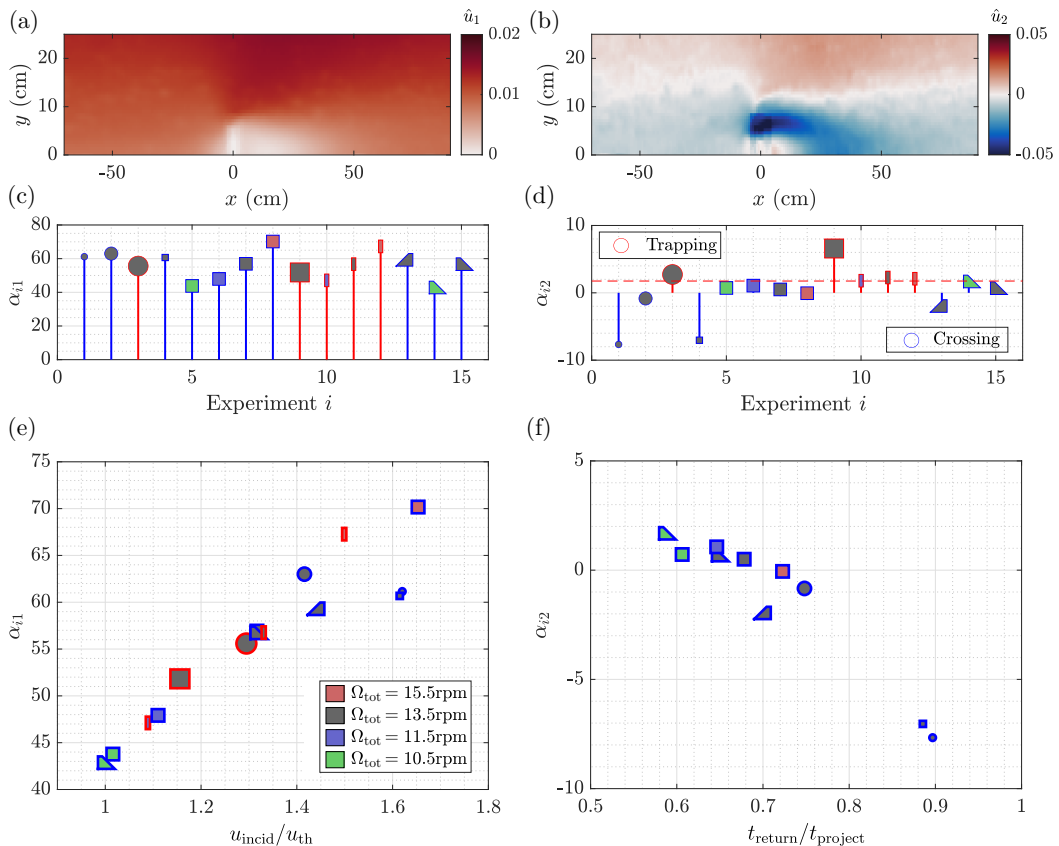
FIG. 12. First two principal modes (a), (c), and (e) $\hat{u}_1$ and (b), (d), and (f) $\hat{u}_2$. (a) The first principal mode is strictly positive and is closely related to the mean flow field. (b) The second principal mode contains a marked flow structure of negative velocity localized near the obstacle. (c) The weights of the first principal component are all positive. (d) The weights of the second principal component correlate with the outcome of the dune-obstacle interaction with high values for the trapping (red outlined symbols) and low values for the crossing events (blue outlined symbols). The symbols are colored with the rotation speeds as shown in Fig. 5(a), with symbol shape and size being related to the particular obstacle used in the relevant experiment. (e) The weights for the first principal component correlate with the incident speed u_{incid}. (f) For the crossing experiments, α_{i2} is negatively correlated with the ratio of the actual return time t_{return} to the projected return time t_{project}. Note that t_{return} is not defined for the trapping events.

and sharp and the sediment flux is less intense. We conjecture that this qualitative statement is generally true for a large class of flows and topographies.

For our specific experiment, we have also managed to develop a quantitative diagnostic whereby the outcome of the dune-obstacle interaction can be predicted from the flow structure around the obstacle in the absence of the dune. Specifically, we performed a modal PCA-based analysis of our data and we have found an interesting correlation between the second principal mode and the outcome of the dune-obstacle interaction. This finding affirms that it is indeed possible to predict the outcome of the dune-obstacle interaction with some confidence by looking at the mean velocity in the absence of sediment. Moreover, it shows the power of the spectral analysis and the importance of the flow structure details near the crest and downstream of the obstacle. The details of our analysis are somewhat specific to the boundary conditions of our setup, but by performing similar studies, e.g., for dunes immersed in a turbulent boundary layer, one may hope to build a predictive library

which encompasses a wide class of geologically relevant cases. This task could be greatly aided by numerical simulations and we would like to hope that the experiments of this paper could be used as a validation benchmark.

[1] F. Charru, B. Andreotti, and P. Claudin, Sand ripples and dunes, Annu. Rev. Fluid Mech. **45**, 469 (2013).

[2] B. Andreotti, Y. Forterre, and O. Pouliquen, *Granular Media: Between Fluid and Solid* (Cambridge University Press, Cambridge, 2013).

[3] K. Kroy, G. Sauermann, and H. J. Herrmann, Minimal Model for Sand Dunes, Phys. Rev. Lett. **88**, 054301 (2002).

[4] K. A. Bacik, S. Lovett, C.-c. P. Caulfield, and N. M. Vriend, Wake Induced Long Range Repulsion of Aqueous Dunes, Phys. Rev. Lett. **124**, 054501 (2020).

[5] W. R. Assis and E. M. Franklin, A comprehensive picture for binary interactions of subaqueous barchans, Geophys. Res. Lett. **47**, GL089464 (2020).

[6] P. Vermeesch, Solitary wave behavior in sand dunes observed from space, Geophys. Res. Lett. **38**, L22402 (2011).

[7] P. Hersen and S. Douady, Collision of barchan dunes as a mechanism of size regulation, Geophys. Res. Lett. **32**, L21403 (2005).

[8] N. Endo, K. Taniguchi, and A. Katsuki, Observation of the whole process of interaction between barchans by flume experiments, Geophys. Res. Lett. **31**, L12503 (2004).

[9] R. D. Lorenz and J. R. Zimbelman, *Dune Worlds: How Windblown Sand Shapes Planetary Landscapes* (Springer, Berlin, 2014).

[10] L. Bruno, M. Horvat, and L. Raffaele, Windblown sand along railway infrastructures: A review of challenges and mitigation measures, J. Wind Eng. Ind. Aerodyn. **177**, 340 (2018).

[11] W. He, N. Huang, B. Xu, and W. Wang, Numerical simulation of wind-sand movement in the reversed flow region of a sand dune with a bridge built downstream, Eur. Phys. J. E **41**, 53 (2018).

[12] A. A. Alghamdi and N. S. Al-Kahtani, Sand control measures and sand drift fences, J. Perform. Constr. Facil. **19**, 295 (2005).

[13] P. L. Barnard, D. M. Hanes, D. M. Rubin, and R. G. Kvitek, Giant sand waves at the mouth of San Francisco Bay, EOS Trans. Am. Geophys. Union **87**, 285 (2006).

[14] A. W. Baar, J. de Smit, W. S. J. Uijttewaal, and M. G. Kleinhans, Sediment transport of fine sand to fine gravel on transverse bed slopes in rotating annular flume experiments, Water Resour. Res. **54**, 19 (2018).

[15] S. B. Dalziel, Decay of rotating turbulence: Some particle tracking experiments, Appl. Sci. Res. **49**, 217 (1992).

[16] B. Andreotti, P. Claudin, and S. Douady, Selection of dune shapes and velocities Part 1: Dynamics of sand, wind and barchans, Eur. Phys. J. B **28**, 321 (2002).

[17] J. F. Kok, E. J. R. Parteli, T. I. Michaels, and D. B. Karam, The physics of wind-blown sand and dust, Rep. Prog. Phys. **75**, 106901 (2012).

[18] S. L. Brunton and J. N. Kutz, *Data-Driven Science and Engineering* (Cambridge University Press, Cambridge, 2019).

[19] M. Horvat, L. Bruno, S. Khris, and L. Raffaele, Aerodynamic shape optimization of barriers for wind-blown sand mitigation using CFD analysis, J. Wind Eng. Ind. Aerodyn. **197**, 104058 (2020).